DNA-relay mechanism is sufficient to explain ParA-dependent intracellular transport and patterning of single and multiple cargos

Ivan V. Surovtsev[a,b,c], Manuel Campos[a,b,c], and Christine Jacobs-Wagner[a,b,c,d,1]

[a]Microbial Sciences Institute, Yale University, West Haven, CT 06517; [b]Department of Molecular, Cellular, and Developmental Biology, Yale University, New Haven, CT 06516; [c]Howard Hughes Medical Institute, Yale University, New Haven, CT 06516; and [d]Department of Microbial Pathogenesis, Yale Medical School, New Haven, CT 06516

Contributed by Christine Jacobs-Wagner, September 28, 2016 (sent for review July 18, 2016; reviewed by Kerwyn Casey Huang, Joe Lutkenhaus, and Ned S. Wingreen)

Spatial ordering of macromolecular components inside cells is important for cellular physiology and replication. In bacteria, ParA/B systems are known to generate various intracellular patterns that underlie the transport and partitioning of low-copy-number cargos such as plasmids. ParA/B systems consist of ParA, an ATPase that dimerizes and binds DNA upon ATP binding, and ParB, a protein that binds the cargo and stimulates ParA ATPase activity. Inside cells, ParA is asymmetrically distributed, forming a propagating wave that is followed by the ParB-rich cargo. These correlated dynamics lead to cargo oscillation or equidistant spacing over the nucleoid depending on whether the cargo is in single or multiple copies. Currently, there is no model that explains how these different spatial patterns arise and relate to each other. Here, we test a simple DNA-relay model that has no imposed asymmetry and that only considers the ParA/ParB biochemistry and the known fluctuating and elastic dynamics of chromosomal loci. Stochastic simulations with experimentally derived parameters demonstrate that this model is sufficient to reproduce the signature patterns of ParA/B systems: the propagating ParA gradient correlated with the cargo dynamics, the single-cargo oscillatory motion, and the multicargo equidistant patterning. Stochasticity of ATP hydrolysis breaks the initial symmetry in ParA distribution, resulting in imbalance of elastic force acting on the cargo. Our results may apply beyond ParA/B systems as they reveal how a minimal system of two players, one binding to DNA and the other modulating this binding, can transform directionally random DNA fluctuations into directed motion and intracellular patterning.

intracellular patterning | active transport | ParA/B system | partitioning | mathematical model

Spatial patterns are omnipresent in biology, spanning a wide range of size scales and organizational levels. At the single-cell level, spatial patterns are readily apparent in the formation of protein gradients and the regular arrangement of cytoskeletal structures, macromolecular complexes, and organelles. Intracellular patterning serves important functions, as it provides a means for cells to organize their intracellular space, sense their geometry, and partition their cellular content (1–5). However, the mechanisms that drive intracellular patterning are often poorly understood.

In this study, we aimed to understand how spatial patterns driven by bacterial ParA/B systems can arise within a small (micrometer-scale) intracellular space dominated by fluctuations and diffusion. ParA/B systems consist of only two proteins, ParA and ParB, that drive the transport and equipartitioning of low-copy-number macromolecular complexes, often referred to as cargos. ParA/B systems are widespread among bacteria (6). For example, many low-copy-number plasmids encode a ParA/B system that distributes plasmid copies at regular intervals along the cell length (7–10). This striking plasmid patterning ensures that division at midcell results in near-equal number of plasmids in each daughter cell. Other ParA/B systems are dedicated to chromosome segregation by transporting origin-proximal DNA regions across the cell (11–14).

ParA/B systems are similar in biochemical properties, suggesting a common mechanism in cargo transport and patterning (13, 15–17). ParA is an ATPase that dimerizes and binds nonspecifically to DNA upon ATP binding. Multiple copies of ParB bind to the cargo and stimulate the ATPase activity of ParA upon interaction. Imaging of fluorescently tagged protein fusions has revealed remarkable correlated localization patterns between ParA and the ParB-rich cargo over the nucleoid region, with the cargo moving in the wake of a "ParA wave" (18–23). In the case of a single-plasmid cargo, the correlated localization dynamics of ParA and ParB results in oscillatory motion of both the cargo and ParA wave over the nucleoid (18, 23, 24).

Although the exact mechanism underlying the ParA/B-driven spatial patterns is not clear, several mechanisms have been proposed. They can be grouped into "filament-based" and "reaction/diffusion-based" models. In the filament-based models, cargos are translocated by depolymerizing filaments of ParA (8, 18, 20, 24–29). However, the polymerizing property of ParA has recently been challenged (30, 31). The reaction/diffusion-based models do not evoke filament depolymerization or any cytoskeletal structure. Instead, they are rooted in the two main properties of the ParA/B system: ParA-ATP dimers bind to DNA and ParB-rich cargo modulates this binding (21, 30, 32–36). Although progress has been made, none of the current models have been

Significance

Although intracellular patterning is crucial for cell function, the mechanisms by which spatial patterns arise often remain elusive. Here, we investigate the mechanism of intracellular patterning by the broadly conserved bacterial ParA/B systems, which drive the transport and partitioning of cellular cargos such as plasmids. We show that a simple model that considers only the known biochemical properties of the ParA and ParB proteins and the stochastic dynamics of chromosomal loci observed in vivo explains the spontaneous formation of propagating protein gradients, cargo oscillations, and equidistant patterns that are characteristic of ParA/B systems. Our study shows that stochastic processes and directionally random forces alone—without cytoskeletal elements or motor proteins—can result in directed motion and complex spatial patterning.

Author contributions: I.V.S. and C.J.-W. designed research; I.V.S. and M.C. performed research; I.V.S. and C.J.-W. analyzed data; and I.V.S. and C.J.-W. wrote the paper.

Reviewers: K.C.H., Stanford University; J.L., University of Kansas Medical Center; and N.S.W., Princeton University.

The authors declare no conflict of interest.

[1]To whom correspondence should be addressed. Email: christine.jacobs-wagner@yale.edu.

This article contains supporting information online at www.pnas.org/lookup/suppl/doi:10.1073/pnas.1616118113/-/DCSupplemental.

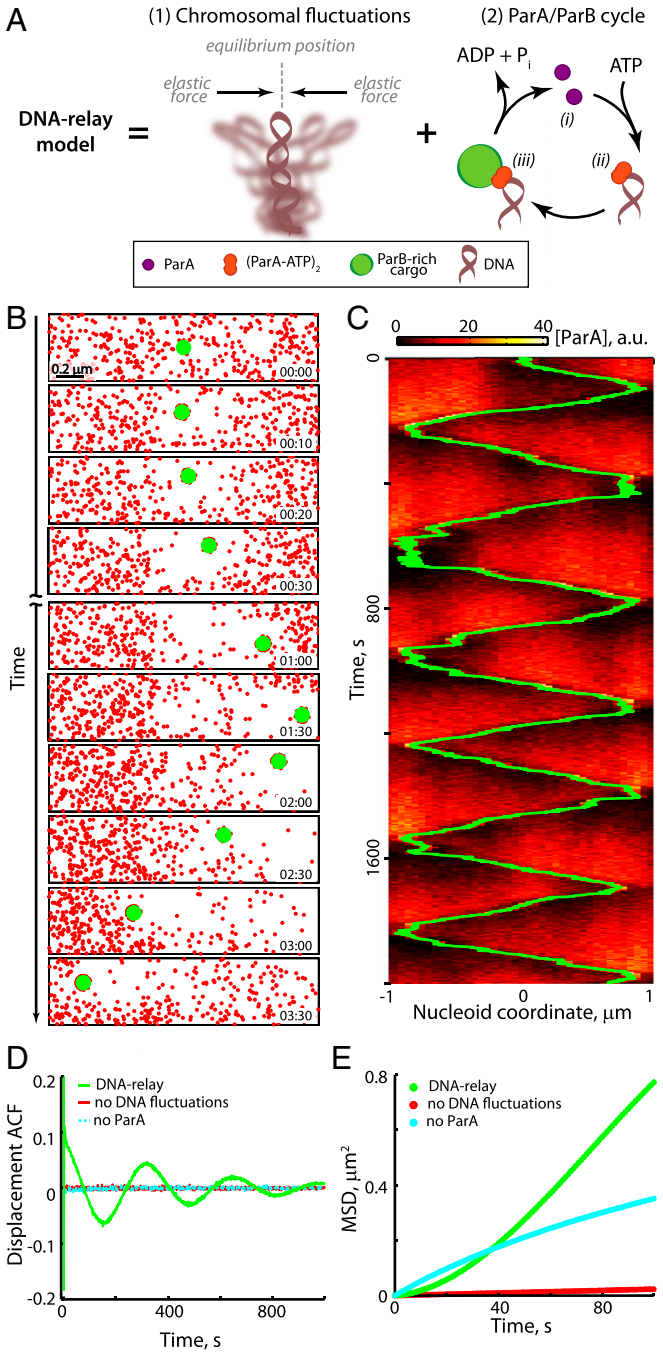

Fig. 1. The DNA-relay model results in oscillations of a single ParB-rich cargo. In silico dynamics of ParA and a single ParB-rich cargo in the DNA-relay model. (*A*) The DNA-relay model is based on known in vivo properties of the chromosome and in vitro biochemical properties of ParA and ParB proteins. (*1*) Chromosomal loci exhibit elastic fluctuating dynamics around their equilibrium position. (*2*) The ParA/ParB cycle is as follows: ATP-bound ParA dimerizes and ParA dimers bind DNA nonspecifically. Cargo-associated ParB stimulates ATPase activity of DNA-bound ParA dimers. ATP hydrolysis disrupts the ParB/ParA/DNA complex by dissolving ParA dimers into monomers. (*B*) Example of dynamics of a single cargo and DNA-bound ParA dimers in simulations of the DNA-relay model, also shown in Movie S1. Shown are snapshots of DNA-bound ParA dimers (red) and ParB-rich cargo (green) positions at indicated times. The size of the cargo and ParA dimers is not drawn to scale. (*C*) Overlay of a one-dimensional cargo trace (position along the nucleoid vs. time) with ParA distribution shown as a kymograph. In *B* and *C*, only DNA-bound ParA dimers are shown, as freely diffusing ParA would display a uniform distribution due to fast diffusion. (*D*) Displacement autocorrelation function (ACF) for simulations of the DNA-relay mechanism; of the diffusion-binding mechanism (the same as the DNA-relay mechanism except that it considers a static chromosome, i.e., no DNA fluctuations); and of a passively diffusing cargo (no ParA). (*E*) Mean square displacements as a function of time for the DNA-relay mechanism, diffusion-binding mechanism (no DNA fluctuations), and passively diffusing cargo (no ParA). In *D* and *E*, ACFs and MSDs are averaged over 128 simulations and are calculated after 600-s transition time from the beginning of simulations. Parameters of the simulation are listed in Table S1.

able to explain all of the various characteristic ParA/B-driven spatial patterns: the asymmetric distribution of ParA, the oscillatory dynamics of single cargos and ParA waves, and the equidistant patterning of multiple cargos.

In the context of a recent study on the *Caulobacter crescentus* ParA/B system that is involved in the translocation of origin-proximal chromosomal regions, our group proposed a diffusion-reaction mechanism, called the "DNA-relay mechanism," in which the translocating force stems from the fluctuating dynamics and elastic properties of the chromosome (31). It is well-known that chromosomal loci display confined motion on the hundred-nanometer scale (37–40). Motion analysis has revealed that confinement is due to an elastic force that brings back chromosomal loci toward an equilibrium position when they fluctuate away from it (31, 37, 38). This observation implies that when ParA dimers bind the DNA, they experience the elastic dynamics of the underlying DNA. In the proposed DNA-relay mechanism, the ParB-rich cargo harnesses the elastic force of the DNA by associating with one or more ParA dimers until ATP hydrolysis occurs (31).

We have shown that a mathematical model of the DNA-relay mechanism can explain the directed transport of chromosomal regions in *C. crescentus* (31). However, it remains unclear whether a DNA-relay mechanism can be applicable to other ParA/B systems. Our original model had several constraints. First, it specifically considered a single-cargo scenario. Second, the cargo was forced to stop after reaching the edge of the nucleoid region to reflect the particular case of chromosomal cargo attachment by the PopZ matrix in *C. crescentus* (41, 42). However, most of ParA-dependent systems involve more than one cargo (e.g., plasmid case), and they typically do not have factors (like PopZ) attaching cargos at specific locations. Third, our model assumed an asymmetric distribution of DNA-bound ParA dimers at time 0 which changed into a progressively steeper gradient during cargo translocation to emulate experimental observations (20–22). Ideally, the asymmetric distribution of ParA should be explained by the model, as we expect this asymmetric pattern to be an intrinsic property of the system. If the DNA-relay mechanism (or any other proposed mechanism) was correct, we would expect it to be applicable to other ParA/B systems and to explain the various ParA/B-driven spatial patterns observed experimentally.

Here, we present a DNA-relay model without the aforementioned constraints and show that a simple DNA-relay mechanism that does not assume cargo attachment or any specific ParA distribution at any given time is sufficient to explain the intracellular patterning of single- and multicargo systems, as well as the spatiotemporal dynamics of its molecular components.

Results

The DNA-Relay Model Results in Oscillatory Motion of Single Cytoplasmic Cargos. To test the hypothesis that a DNA-relay mechanism can explain the different spatial patterns driven by ParA/B systems, we considered a stripped-down version of the DNA-relay model that only includes the known ParB-dependent ATPase cycle of ParA and the demonstrated elastic dynamics of the chromosome (Fig. 1*A*). Specifically, in the model, ParA is in one of three possible states (Fig. 1*A*): (*i*) a freely diffusing ParA, (*ii*) DNA-bound ParA-ATP dimer, or (*iii*) DNA-bound ParA-ATP dimer engaged in complex with ParB on the surface of the cargo.

ParA-ATP dimers in both DNA-bound states (*ii* and *iii*) experience two types of forces: random Brownian forces from the cytoplasmic environment that cause random fluctuations of the ParA/DNA complex around its mean position in the cell, and an elastic force from the underlying DNA that returns the ParA/DNA complex to the mean position. The ParB-rich cargo diffuses but, when engaged with one or more DNA-bound ParA-ATP dimers, it also experiences the sum of elastic forces from each ParB/ParA/DNA complex. In this complex, ParB stimulates ATP hydrolysis, releasing ParA from the DNA. If all ParB interactions with ParA-ATP dimers are disrupted, the cargo moves only by diffusion. Free ParA can redimerize and rebind to DNA anywhere with uniform probability. This random rebinding to the DNA takes into account the fast diffusion of cytoplasmic ParA before DNA binding.

We performed 2D Brownian dynamics simulations with parameters constrained by values determined experimentally for plasmid systems in *Escherichia coli*. Because plasmids interact with ParA only when ParA is bound to the DNA and because plasmids are known to remain within the nucleoid region (18, 24), we chose the dimensions of the simulation box so as to reflect the nucleoid area (2 × 0.5 μm) in the cell, which we determined by quantitative fluorescence microscopy of DAPI-stained *E. coli* cells grown in M9 glucose at 30 °C (Fig. S1*A*). We estimated the diffusion coefficient of plasmids (D = 0.003 μm^2/s) from the passive motion of pB171-derived plasmids that lack the ParA/B system (Fig. S1*B*). To estimate the local energy potential that individual ParA-ATP dimers experience when bound to the DNA, we tracked the motion of single fluorescently labeled DNA loci in *E. coli* cells. As in *C. crescentus* (31), the probability of finding a chromosomal locus away from its mean position was very well described by an asymmetric 2D-Gaussian (Fig. S1*C*), with standard deviations σ_x = 0.1 μm and σ_y = 0.05 μm along the cell length and width, respectively. The asymmetry in locus motion may reflect an asymmetry in the local DNA architecture relative to the long and short axes of the cell. Importantly, the fact that the distribution is Gaussian indicates that the locus moves in harmonic (elastic) potential. This analysis allowed us to estimate the effective elastic constants of the *E. coli* chromosome, $k_{spX}/(kT) = 1/\sigma_x^2$ and $k_{spY}/(kT) = 1/\sigma_y^2$ along the long and short cell axes, respectively (k is the Boltzmann constant and T is the absolute temperature). We used k_{hyd} = 0.1 s^{-1} for the rate constant of ParB-stimulated ATP-hydrolysis and $k_{db} = k_{hyd}$ for the rate constant of ParA rebinding to DNA after the ATP hydrolysis based on in vitro studies (30, 43). We did not consider spontaneous (without ATP hydrolysis) dissociation between ParA dimers and the ParB-rich cargo because it has been shown to be very slow (>10 min) (33). The size of a ParA dimer and ParB-rich cargo were set to 4 and 100 nm, respectively, to match values reported elsewhere (31, 44).

To start with unbiased conditions, simulations were initiated with a freely diffusing ParB-rich cargo at the center of the nucleoid box and with DNA-bound ParA dimers uniformly distributed throughout the nucleoid. Remarkably, simulations showed that the stripped-down DNA-relay model (i.e., in the absence of a pre-established ParA gradient) resulted in spontaneous motion of the ParB-rich cargo toward one end of the nucleoid (Fig. 1*B*). Once near the end, the cargo changed direction and moved toward the other end, leading to back-and-forth motions over the nucleoid (Movie S1 and Fig. 1*C*). This near-oscillatory motion was accompanied by the redistribution of the DNA-bound ParA (Fig. 1 *B* and *C*) due to dissociation of ParA from the DNA after ATP hydrolysis stimulated by the ParB-rich cargo. These dynamics and the time scale of the oscillation period are in good agreement with what has been reported for single-plasmid cargo in *E. coli* (18, 23, 24). As in experiments (23), the oscillatory motion of individual cargos was not perfectly periodic (Fig. 1*C*), which was also apparent at the population level by the dampening in displacement autocorrelation function (Fig. 1*D*). Importantly, this near-oscillatory behavior was completely abolished when chromosomal fluctuations or ParA were removed from simulations (Movies S2 and S3 and Fig. 1*D*). This result is in agreement with experiments showing that plasmid and ParA wave oscillations require both ParA and ParB, as well as the ability of ParA to bind the DNA (18, 45).

An important experimental observation made by the Gerdes and Howard groups is that the ParA/B system causes the plasmid cargos to move faster than if they were passively diffusing, as shown by mean square displacement (MSD) analysis that compares the motion of plasmids with and without a ParA/B system (28). Consistent with this experiment-based conclusion, MSD analysis of our simulated data showed that ParA-driven motion is much faster (i.e., displays bigger displacements) than purely diffusive motion (no ParA) (Fig. 1*E*). Note that, on short time scales, diffusion is always faster than active transport, regardless of the underlying active transport mechanism. The cross-over time when active transport becomes more efficient than diffusion depends on the diffusion coefficient of the cargo and on the velocity of the transport. For example, for a diffusion coefficient of cargo D = 0.003 μm^2/s (as measured here), the cross-over time is 40 s (Fig. 1*E*). When we performed simulations with D = 0.0003 μm^2/s to match the value reported by the Gerdes and Howard groups (28), the cross-over time is ∼2 s (Fig. S2*A*), after which the DNA-relay mechanism becomes more efficient than diffusion. The smaller D value still resulted in robust oscillatory motion of individual cargos, in a manner that depended on chromosome fluctuations and ParA/ParB interactions (Fig. S2*B*).

Removing the chromosomal fluctuations from the simulations while keeping the ParA/ParB interactions led to cargo motion much slower than free diffusion (Fig. 1*E* and Fig. S2*A*), simply because the diffusion of the cargo is repeatedly interrupted by its interaction with static ParA bound to the DNA. This result indicates that a simple reaction-diffusion model—called "diffusion-ratchet" (30) or "diffusion-binding" model (31)—that only evokes cargo diffusion and the known ParA/ParB interactions is not sufficient to explain directed plasmid motion. A translocating force such as the existing chromosomal fluctuations must be present to obtain active motion.

Directional Motion Is Achieved Through ParA Depletion and Stochastic Symmetry Breaking. In our simulations of the DNA-relay model, the distribution of DNA-bound ParA dimers is symmetric at time 0 (Fig. 2 *A* and *B*, *Top*, and *C*, state 0). How can a gradient of DNA-bound ParA dimers and directional motion of a cargo arise in such a symmetric system? Plotting both the instantaneous position (Fig. 2*A*) and the equilibrium position (Fig. 2*B*) of DNA-bound ParA dimers at a given time revealed that at the beginning of the simulations, ParA dimers near the ParB-rich cargo can reach and interact with the cargo due to their fluctuating dynamics (Fig. 2 *A* and *B*). Interaction with the cargo captures the DNA-bound ParA dimers in a "stretched" state, away from their equilibrium position (Fig. 2*C*, state 1), creating a depletion of ParA dimers around the cargo and a corresponding accumulation of ParA dimers at the cargo (Fig. 2 *A* and *B*, second and third panels). Such ParA depletion around the cargo has been described as a key event preceding cargo motion in in vitro reconstitution experiments with ParB-coated beads on ParA-bound DNA carpets (33, 46). Our simulations suggest that this characteristic ParA depletion corresponds to DNA-bound ParA dimers in a stretched configuration.

At first, in our simulations, the ParA depletion is symmetric reflecting that a similar amount of ParA dimers interact with the cargo from both sides, thus resulting in near-zero net force (Fig. 2*C*, state 1), akin to the initial situation in a tug-of-war game. As a result, the cargo does not display any significant translocation. Stochasticity of ATP hydrolysis breaks the symmetry: on ATP hydrolysis (happening randomly on one side of the cargo earlier

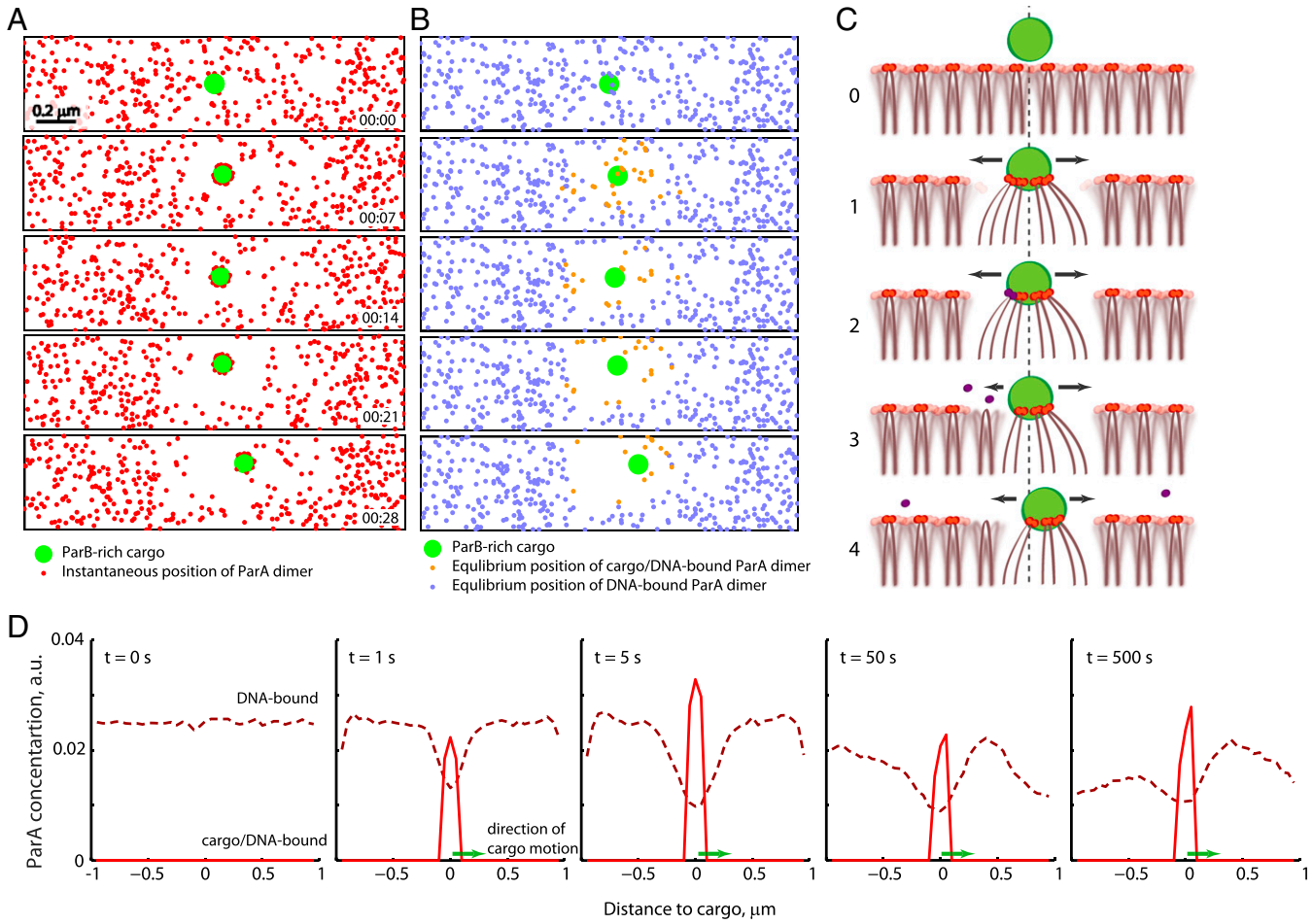

Fig. 2. Symmetry breaking and formation of propagating ParA wave through interaction of ParB-rich cargo with fluctuating DNA-bound ParA dimers. Initial stages of the ParA/B system dynamics in the DNA-relay model. (*A*) Example of the cargo (green) motion and ParA dimer (red) positions at initial stages of simulations. The size of the cargo and ParA dimers is not drawn to scale. (*B*) Equilibrium positions of the ParA dimers from *A* that are either bound to DNA only (blue) or to the DNA and cargo (orange). (*C*) Schematic of ParA depletion formation around the cargo and of symmetry-breaking due to the stochastic nature of ATP hydrolysis. The dashed line shows the initial position of the cargo. See text for details about each stage (0–4). (*D*) Distribution of DNA-bound (dashed curve) and cargo/DNA-bound (solid curve) ParA dimers relative to the cargo motion at initial stages of the simulations. To generate the plot, the position of the cargo served as a center of coordinate while the direction of cargo motion (with $dt = 1$ s) specified a positive direction of the coordinate axes in each individual simulation at the indicated moment of time. ParA distributions were calculated in these coordinates and averaged over 500 simulations.

than on the other; Fig. 2*C*, state 2), the net force becomes unbalanced (Fig. 2*C*, state 3), resulting in incremental cargo motion to the side opposite of where ATP hydrolysis just happened (Fig. 2*C*, state 4). Direction of the cargo motion is determined spontaneously. Accordingly, the cargo started to move to the left of the simulation box in approximately half of simulations (57 of 120), whereas it moved to the right in the remaining simulations.

As shown in Fig. 2*D*, cargo translocation makes the local depletion of ParA asymmetric, with more ParA dimers in front of the cargo (in the direction of the motion). As a result, there are more DNA-bound ParA dimers that can reach and grab the cargo on that side, resulting in additional force in the same direction. Concomitantly, the depletion zone behind the cargo becomes larger with fewer ParA dimers able to reach the cargo from that side (Fig. 2 *A* and *B*, *Bottom*, and *D*, $t = 500$ s). Thus, the interaction of the ParB-rich cargo with the initial symmetric field of DNA-bound ParA dimers, together with the stochastic nature of the ATP hydrolysis, creates a wave of DNA-bound ParA dimers (Fig. 2*D*). Note that there is also a characteristic depletion of ParA right in front of the cargo, which reflects DNA-bound ParA dimers in a stretched configuration (away from their equilibrium position) through their interaction with ParB on the surface of the cargo (Fig. 2*D*). The elastic force that brings the DNA-bound ParA dimers toward their equilibrium position results in a net pulling force from the ParA wave. Motion of the cargo toward the ParA wave leads to a redistribution of ParA, propagating the ParA wave forward (Fig. 2*D*). Repetition of this process creates a continuous motion of the cargo in the wake of a ParA wave.

We found that the number of ParA dimers interacting with the cargo fluctuates, but rarely goes to zero (Fig. 3*A*). This observation means that the cargo is almost always associated with the DNA via ParA dimers; i.e., the cargo is rarely released to freely diffuse. Thus, on average, the cargo is being relayed from one DNA region to the next. This DNA relay continues toward the same direction until the cargo reaches the end of the nucleoid and changes direction.

Note that, in the DNA-relay mechanism, the asymmetric distribution of ParA is dynamic, as it keeps changing as the cargo moves. This dynamic ParA gradient is distinct from the special case of the steady-state gradient of ParA that is maintained without cargo motion throughout the G1 phase of *C. crescentus* during which the cargo is physically anchored to a cell pole (20–22, 41, 42). Steady-state gradient formation, which originates

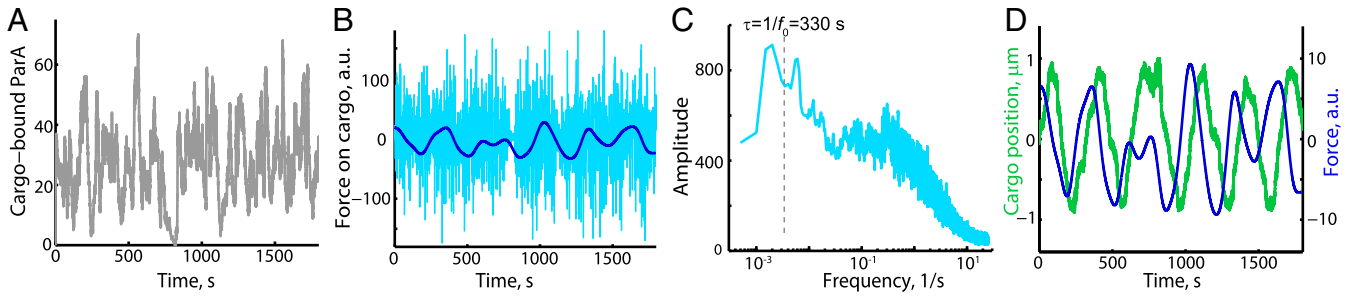

Fig. 3. Stochastic forces underlie the directed motion of the cargo. (*A*) Number of DNA-bound ParA dimers associated with the cargo as a function of time in a simulation of the DNA-relay model. (*B*) Instantaneous net elastic force on the cargo from the chromosome as a function of time in the same simulation. The navy blue curve corresponds to the time-averaged elastic force (with the Gaussian weights, $\tau = 40$ s). (*C*) Fourier spectrum of the elastic force on the cargo. Dashed line denotes the frequency corresponding to the average period of oscillations. (*D*) Position of the cargo along the nucleoid length and the time-averaged elastic force as a function of time.

from rare spontaneous (without ATP hydrolysis) dissociation of ParA dimers from DNA, requires minutes to develop (47). This time is too long for this mechanism to play a significant role during cargo translocation, as the cargo crosses the entire nucleoid on this time scale.

Stochastic Forces from the Chromosome Drive the Translocation of the Cargo. Active transport requires a sustained translocating force. In the DNA-relay model, the only forces the cargo experiences are random uncorrelated forces from the cytoplasmic environment and elastic forces from the chromosome. The former results in Brownian motion (e.g., no ParA case in Fig. 1*D*), whereas the latter is responsible for directed translocation. The instantaneous elastic force acting on the cargo is very stochastic (Fig. 3*B*). The stochasticity is due in part to the large fluctuations in number of ParA bound to the cargo (Fig. 3*A*), and in part to the random displacements of the cargo by stochastic Brownian forces.

Fourier analysis of the force on the cargo shows a strong low-frequency peak that reflects an underlying frequency of the long-time-scale oscillatory dynamics of the cargo (Fig. 3*C*). The dashed line in Fig. 3*C* marks the frequency (f_0) corresponding to the average period of the cargo oscillations ($\tau = 1/f_0 = 330$ s). Although the instantaneous force is stochastic in amplitude and direction, time-averaging reveals a nonzero force component with a near-oscillatory time dependence (navy blue line in Fig. 3*B*) that is positively phase-shifted relative to the cargo coordinates (Fig. 3*D*). We note, however, that the correlation between the time-averaged force and the cargo trajectory is not always perfect, as it can be seen during the 600- to 700-s window in Fig. 3*D*. Such deviations are manifestations of the highly stochastic nature of the force. Indeed, the deviation in the 600- to 700-s window disappeared when we reduced the influence of sporadic, most deviant individual forces by plotting the median force (Fig. S3). Altogether, our data show that highly stochastic force can result in directed motion.

When Two Cargos Are Present, the DNA-Relay Mechanism Results in Effective Repulsion Between Approaching Cargos. The small depletion of ParA in front of the moving cargo (Fig. 2*D*) causes the cargo to change direction before it reaches the end of the nucleoid (Fig. 1*C*). This small front depletion leads to another important consequence when more than one cargo is present. When two cargos are approaching each other, their front depletion zones coalesce into a large depletion zone. As a result, there are no longer ParA dimers in front of the cargos that can sustain the direction of the motion. To illustrate this expectation, we simulated dynamics of two ParB-rich cargos in a narrower (0.3 μm instead 0.5 μm) simulation box to increase the probability of cargo running into each other (Movie S4). Kymographs showing the position of the two cargos in relation to the distribution of ParA dimers over time clearly demonstrated that every time the two cargos came close to each other, a large depletion zone formed between them (Fig. 4*A*). The depletion, in turn, caused an apparent repulsion and change of cargo direction. In the DNA-relay model, the mode of the individual cargo motion within their soft boundaries is similar to the near-oscillatory dynamics of a single cargo. This localized near-oscillatory behavior disappeared if the DNA fluctuations were not considered (Movie S5) or if there was no ParA (Movie S6). Thus, both the ParA/cargo interaction and the chromosomal fluctuations are required for oscillations.

It is important to note that the DNA-relay model does not include any cargo–cargo interactions. Our model only considers cargo–ParA interactions. Calculations of the average force experienced by the cargos showed a strong dependence of the force on the distance between cargos (Fig. 4*B*), with a repulsive force quickly increasing when the cargos were separated by less than 0.4 μm along the long axis. This length is consistent with the length of the merged ParA depletion zone ($2 \times \sim 0.2$ μm) in front of the cargos. The repulsion comes from the collective effect of individual cargos interacting with ParA dimers. This short-range repulsion leads to localized oscillations of each cargo within separate regions of the nucleoid, although the boundaries of these regions are "soft," as they change according to the cargo dynamics (Fig. 4*A* and Movie S4).

For Multiple ($n > 2$) Cargos, the Effective Repulsion Between Cargos Leads to Equidistant Patterning. It is common for ParA/B systems to have more than two cargos. For example, under our experimental conditions, the most prevalent number of pB171-derived plasmids per *E. coli* cell is four, consistent with a previous report (18). When we performed simulations with four cargos that are localized at the center of the nucleoid at time 0, we found that the cargos dispersed very quickly after simulations began (Fig. 5*A* and Movie S7). From then on, the cargos displayed stable back-and-forth motion within narrow regions, leading to near equidistant cargo distribution along the nucleoid (Fig. 5*A* and Movie S7).

The cargos displayed perfect repulsion when the width of the simulation box was 0.3 μm. Increasing the width to 0.5 μm to more accurately reflect the size of the nucleoid under our experimental conditions (Fig. S1*A*) resulted in less confined cargo motion, with occasional "cross-overs" of cargos along the long axis of the nucleoid (Movie S8). The cross-overs occurred simply because the repulsion occurs only at a certain range (Fig. 4*B*), and a wider simulation box allowed cargos to occasionally go around each other without coming in contact (Movie S8). Despite cargo confinement not being perfect, the range of repulsion was still sufficient to produce equidistant cargo distribution on time average (Fig. 5*B*). For comparison with experiments, we monitored the motion of the pB171-derived plasmids in *E. coli*

cells (Movie S9). The plasmids displayed behavior very reminiscent of the simulations—they were very dynamic and their distribution was regularly spaced when averaged over time (Fig. 5*B*), consistent with previous reports (7–10).

We hypothesized that this near-equidistant distribution of plasmids in real cells is also driven by the cargo–cargo repulsion that we observed in our simulations (Fig. 4*B*). This repulsion stems from the ParA depletion in the zone between two nearby cargos, which is evident in simulations by the nonlinear dependence of the ParA amount on the distance between cargos (Fig. 5*C*). When we measured ParA-GFP signal between neighboring plasmids in *E. coli* cells as a function of the distance separating these plasmids, we observed a similar nonlinear dependence (Fig. 5*D*), consistent with our hypothesis.

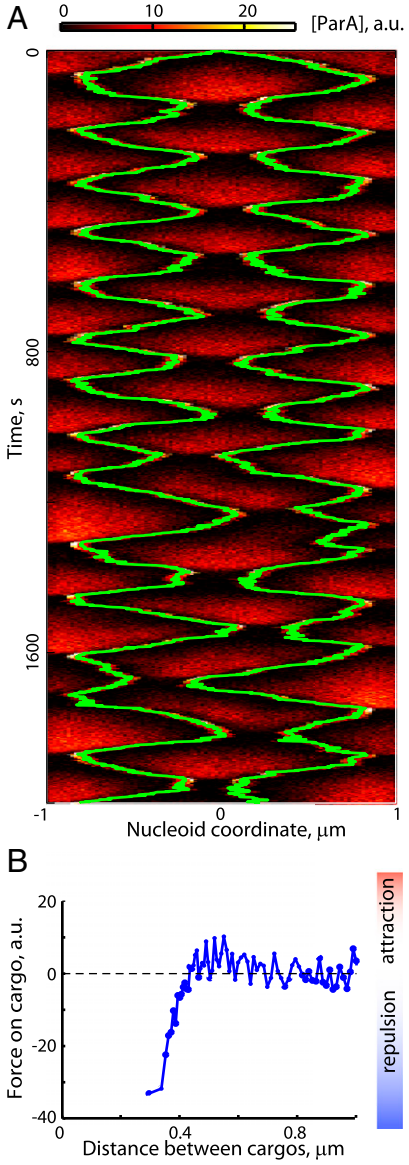

Fig. 4. The DNA-relay mechanism leads to a repulsion between cargos. Simulation of the DNA-relay model of two ParB-rich cargos in a 0.3-μm-wide nucleoid box. (*A*) Depletion of ParA dimers between approaching cargos results in a change of cargo direction. Shown is a kymograph of cargo traces (green) overlayed with ParA dimers distribution (red), also shown in Movie S4. (*B*) Average (over 24 simulations for 2,000 s, after 600-s transition time) force on the cargos as a function of intercargo distance.

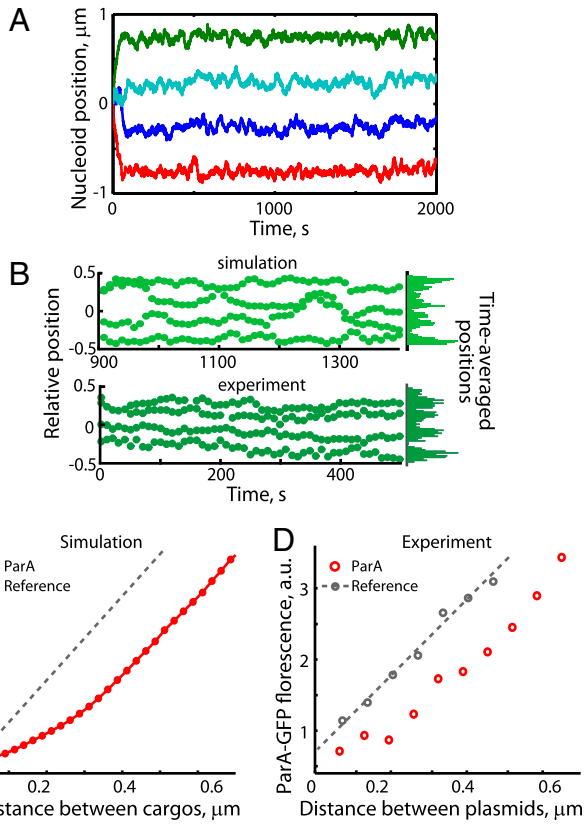

Fig. 5. The DNA-relay model results in time-averaged equidistant distribution of multiple cargos. (*A*) Representative traces of four cargos in a simulation of the DNA-relay model with a 0.3-μm-wide nucleoid, also shown in Movie S7. (*B*) Comparison between the in silico cargo dynamics (with nucleoid width of 0.5 μm as measured in vivo) and the in vivo motion of pB171-derived plasmids (pSR320) in *E. coli* cells (strain KG22) in the case of four cargos/plasmids. Shown are the relative positions of the cargos/plasmids vs. time and their distributions averaged over the shown period. The simulation trajectories are plotted after a 900-s transition period. (*C*) Plot showing the ParA amount between cargos as a function of the intercargo distance in simulations ($n = 128$) of the DNA-relay model for four cargos and 0.5-μm-wide nucleoid. The dashed line shows a linear relationship for reference. (*D*) Signal quantification of ParA-GFP and DAPI signals between neighboring plasmids as a function of interplasmid distance in DAPI-stained *E. coli* cells (KG22 strain harboring pB233 plasmid) with four plasmids per cell ($n = 381$). The DAPI data (circles, experimental values; line, linear fit) provide a reference for uniform DNA binding.

The DNA-Relay Model Is Compatible with 3D Cargo Motion Through the Nucleoid Volume. It was recently demonstrated by 3D superresolution microscopy that ParA/B-dependent plasmids are found within the volume of the nucleoid, as opposed to on their surface (36). Given this important experimental observation, we also modeled the DNA-relay mechanism in 3D, simulating the cargos and ParA dynamics within a spherocylinder-shaped nucleoid (length = 2 μm, diameter = 0.5 μm). We found that our main conclusions remain valid even when the 3D geometry of the nucleoid is considered. Indeed, the 3D model led to oscillations of single cargos and correlated ParA waves (Movie S10 and Fig. 6*A*). Simulations with four cargos (Movie S11) resulted in dynamic equidistant patterning of cargos (Fig. 6 *B* and *C*), associated with a nonlinear ParA distribution between cargos (Fig. 6*D*).

Discussion

We show here that the DNA-relay model—whether the motion of the cargo occurs on a surface (in 2D) or throughout the volume of the nucleoid (in 3D)—reproduces the signature behaviors of ParA/B systems: oscillations of single cargos, propagating

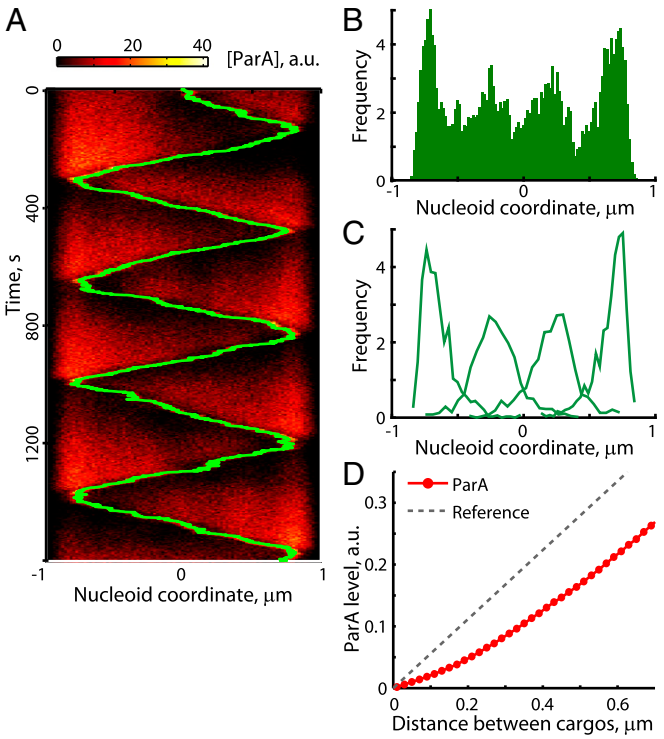

Fig. 6. 3D DNA-relay model reproduces cargo and ParA dynamics. Results of 3D simulations of the DNA-relay model with a spherocylinder-shaped nucleoid (2 μm length and 0.5 μm diameter). (*A*) Example of dynamics of a single cargo (green) and distribution of DNA-bound ParA dimers (red) in 3D simulations of the DNA-relay model, also shown in Movie S10. (*B*) Histogram of cargo positions after a 100-s transition period in the four-cargo simulation shown in Movie S11. (*C*) Distribution of the four cargos in the 3D DNA-relay model averaged over 120 simulations after a 600-s transition period. (*D*) The ParA amount between cargos as a function of the intercargo distance in 3D simulations of the DNA-relay model for four cargos (n = 120). The dashed line shows a linear relationship for reference.

ParA waves correlated with cargo motion, and equidistant distributions of multiple cargos. The model relies only on known properties, namely, the ParA/ParB biochemistry and the chromosomal fluctuations. Our results imply that these properties, which are stochastic in nature, are sufficient to create directed motion and to change a homogenous environment into spatial patterns.

A well-studied spatial oscillator in bacteria is the MinD/E system, which plays an important role in division site selection (48–51). The biochemical similarities between the MinD/E and ParA/B system are striking: upon binding to ATP, MinD dimerizes and binds to the membrane, whereas MinE stimulates MinD ATPase activity, which, in turn, releases MinD from the membrane. From a biochemical perspective, the only apparent difference with the ParA/B system is the binding surface, which is the DNA for ParA as opposed to the membrane for MinD. However, the mechanism of action between these two systems is fundamentally different. The MinD/E system does not rely on any known translocating force besides the passive transport (diffusion) of MinD and MinE (52, 53). In contrast, the DNA-relay model is based on an active transport that harnesses the elastic dynamics of the chromosome to translocate the ParB-rich cargo. A key difference between the two systems is the size scale of what is transported. In the case of MinD/E, there is no cargo to move; only proteins move and they can diffuse across the cell in less than a second because of their small size. ParA/B systems, on the other hand, move large cargos, which, without a ParA/B system, would take on the scale of 10 min to diffuse across the cell. When chromosomal fluctuations are not included in simulations (i.e., only diffusion and ParB/ParA interactions are considered), there are no cargo oscillations (Fig. 1*D*; Movie S1 vs. Movie S2) or spatial patterning (Movie S4 vs. Movie S5).

ParA-dependent systems are widespread in bacteria. Interestingly, some of them do not have an associated ParB homolog. For example, such ParA-dependent systems have been shown to drive the equidistant patterning and partitioning of non-DNA cargos such as chemotaxis protein clusters and metabolic protein organelles (54, 55). Although these ParA-dependent systems do not have a ParB protein, their partitioning function still requires a partner protein associated with the cargo (56, 57). Thus, a DNA-relay mechanism may still be at play. It will be interesting to see whether the partner protein plays a ParB-like function by modulating the lifetime of ParA association to the DNA.

An important aspect of this study is that all parameters in the simulations were constrained by values derived from experiments; there was no parameter optimization. Because ParA/B systems are involved in the transport of cargos of different sizes with correspondingly different diffusion coefficients, we varied the diffusion coefficients to encompass the range of values (0.0001–0.03 $\mu m^2/s$) that have been reported for ParA/B cargos (28, 31, 58). We found that the DNA-relay model is robust over these 100-fold variations in diffusion coefficients with respect to cargo inheritance in daughter cells (Fig. S4). The DNA-relay model also performed well over the wide range of ParA dimer copies (100–4,000) per cell (Fig. S4) that have been reported in the literature (8, 28, 31). We also show that the DNA-relay mechanism can accommodate different cargo numbers. Thus, the DNA-relay mechanism we propose is robust to variations among ParA/B systems.

In the DNA-relay model, the cargo translocation is driven by intrinsic chromosomal fluctuations. These chromosomal dynamics contribute to the transport mechanism in two ways. First, they provide an elastic force on the cargo. Second, they allow DNA-bound ParA dimers to explore space around their equilibrium position, thus expanding the zone of ParA-cargo interaction. The size of the interaction zone is dictated by the amplitude of the fluctuations and reflects the size of the ParA-depletion zone. The simplicity and efficiency of the DNA-relay mechanism makes it, at least in principle, broadly applicable, perhaps even beyond ParA-dependent systems. Elastic dynamics of fluctuating chromosomal loci were observed not only in different bacteria (31) (Fig. S1*C*), but also in eukaryotic nuclei by tracking fluorescently labeled chromosomal loci (59). Therefore, these elastic dynamics likely represent a universal feature of compacted, high-order structured DNA. The DNA-relay model shows that a simple biochemical system with only two players—one binding to the DNA and the other modulating this binding—can harness the fluctuations of the DNA, which are random in direction, to spontaneously generate directional motion and spatial patterning inside the cell.

Materials and Methods

Strains and Culture Conditions. To measure chromosomal locus dynamics, we used *E. coli* strain CJW4473 (DL2875/pMC1), which encodes a *tetO* array at the *cynX* locus (60) and harbors pMC1 plasmid carrying *mcherry* and a *tetR-yfp* fusion. To construct pMC1 plasmid, *lacI-cfp* was removed from pLAU53 (61) by digestion with EcoRI. Then, *mcherry* was amplified from pCHYC-2 (62) by PCR (using primers TCGTTCTAGAATGGTGAGCAAGGGCGAGGAGG and AGGTTCTAGATTACTTGTACAGCTCGTCC) (62) and then inserted at the NheI site. After construction, pMC1 was verified by PCR and fluorescence microscopy.

To track the motion of pB171-derived plasmids, we used *E. coli* strain KG22 harboring a dual plasmid system (18). The first plasmid, pSR124 (18), encodes an inducible *tetR-mcherry* fusion to visualize the second plasmid that was pSR233 (*par+*) or pSR230 (*par–*). Plasmid pSR233 is a miniR1 plasmid that carries a pB171-derived *par2* locus (45), a *tetO* array, and a *parA-gfp* fusion (18). pSR230 is essentially the same, with the exception that it does not encode the *par2* locus (18).

Cell cultures were grown overnight at 30 °C to $OD_{600} < 0.25$ in M9 medium (0.87 g/L Na_2HPO_4, 0.54 g/L KH_2PO_4, 0.50 g/L NH_4Cl, 0.5 mM $MgSO_4$, 0.5 mM $CaCl_2$, 0.01 mM $FeSO_4$) supplemented with 0.2% (wt/vol) glycerol, 0.06% (wt/vol) casamino acids, and thiamine (1 μg/mL). To track chromosomal locus dynamics, synthesis of TetR-mCherry was induced with 0.02% arabinose (wt/vol). Cells then were grown for 45 min at 30 °C before imaging. For plasmid tracking, synthesis of TetR-mCherry was induced for 60 min at 30 °C following the addition of 0.3% arabinose. After the induction, cells were washed with M9 + 0.2% (wt/vol) glucose medium (also supplemented with casamino acids and thiamine) and grown for 4–5 h at 30 °C before imaging to dilute TetR-mCherry level through growth and division to prevent plasmid clustering. All strains were initially grown overnight in the presence of antibiotics (100 μg/mL ampicillin for the strain carrying pMC1 and 100 μg/mL ampicillin plus 50 μg/mL kanamycin for strains carrying pSR230 and pSR233) that were omitted during subsequent induction, regrowth, and imaging steps.

Microscopy and Image Processing. For imaging, cells were spotted on 1% agarose pads containing M9 glucose medium and imaged after 30 min at room temperature on an Eclipse Ti-E microscope (Nikon) system with a 100×/1.40 NA phase-contrast objective (Plan Apochromat; Nikon) and an Orca-II-ER camera or an ORCA-Flash4.0 V2 Digital CMOS camera (both Hamamatsu Photonics) combined with a Perfect Focus System (Nikon). Microscope and image acquisition were controlled by MetaMorph software (Molecular Devices). Cell outlines, segmentation, fluorescence quantification, object (nucleoid) detection, and spots detection (plasmid localization) were carried out using Oufti (63) and MicrobeTracker (64). We estimated the localization error for the detection of fluorescent spots (plasmids or chromosomal loci) to be about 20 nm (65).

Quantitative Image Analysis. To determine the dimensions of individual nucleoids, cells were stained by addition of 1 μg/mL DAPI to cell cultures for 5 min before spotting cells on the pad. A standard object detection output from Oufti was used for quantification (63). We defined the length of the nucleoid by projecting image coordinates of all vertices of the nucleoid outline on the cell centerline and by calculating the difference between minimal and maximal values. Width of the nucleoid was defined as an area of the nucleoid (standard field returned by Oufti in object output) divided by the length of the nucleoid.

To track the motion of chromosomal loci, spots detected by spotFinder (an auxiliary function of MicrobeTracker (64) were connected into trajectories for cells with a single spot per cell. Then, we determined, in cellular coordinates (along short and long cell axes), the mean position of each trajectory and the positions of each spot relative to the trajectory's mean position. Combined distributions of positions relative to the mean trajectory position were generated (as in Fig. S1C) and fitted by a Gaussian with width σ. According to Boltzmann distribution, a probability P to observe a given state is proportional to $\exp(-E/kT)$, where E is the energy of state, k is the Boltzmann constant, and T is the absolute temperature. Hence, a Gaussian distribution is expected for deviations from the mean position for a chromosomal locus in a harmonic potential, i.e., for a particle under an elastic force with $E = k_{sp}(x - x_0)^2/2$. The underlying elastic constant k_{sp} was calculated as $k_{sp} = kT/\sigma^2$.

To track the motion of multiple plasmids, identified spots were connected between frames into a trajectory by minimizing the displacement of individual spots. If the displacement exceeded the maximum allowed value, a new trajectory was started. Then, MSDs were calculated in the ensemble-averaged sense as follows:

$$MSD(t) = \frac{1}{n}\sum_{i=1}^{n}[x_i(t) - x_i(0)]^2, \quad [1]$$

where $x(t)$ is the coordinate of a given particle at moment t, $x(0)$ is the coordinate of this particle at the beginning of the trajectory, and n is the number of trajectories.

To quantify ParA-GFP fluorescence as a function of the interplasmid distance, the closest neighboring plasmid was first identified for each plasmid in the cell. Then, the amount of fluorescence within this plasmid–plasmid segment of the cell was calculated from the standard fluorescence profile output from Oufti. Finally, the data were binned according to interplasmid distance, and the average values for each bin were quantified.

Model Simulations. Briefly, Brownian dynamics simulations of cargos and ParA dynamics within simulation boxes were carried out using a second-order approximation (66) and parameter values derived from experiments (Table S1 and *Supporting Information*).

ACKNOWLEDGMENTS. We thank Drs. Kenn Gerdes, David Sheratt, and David Leach for kindly providing bacterial strains. We also thank all the members of the C.J.-W. laboratory for fruitful discussions over the course of the study and for critical reading of this manuscript. This work was funded in part by NIH Grant R01 GM065835. C.J.-W. is a Howard Hughes Medical Institute investigator.

1. Fuller BG (2010) Self-organization of intracellular gradients during mitosis. *Cell Div* 5(1):5.
2. Howard M (2012) How to build a robust intracellular concentration gradient. *Trends Cell Biol* 22(6):311–317.
3. Bement WM, von Dassow G (2014) Single cell pattern formation and transient cytoskeletal arrays. *Curr Opin Cell Biol* 26:51–59.
4. Griffin EE (2015) Cytoplasmic localization and asymmetric division in the early embryo of Caenorhabditis elegans. *Wiley Interdiscip Rev Dev Biol* 4(3):267–282.
5. Wingreen NS, Huang KC (2015) Physics of Intracellular Organization in Bacteria. *Annu Rev Microbiol* 69:361–379.
6. Livny J, Yamaichi Y, Waldor MK (2007) Distribution of centromere-like parS sites in bacteria: Insights from comparative genomics. *J Bacteriol* 189(23):8693–8703.
7. Ebersbach G, Sherratt DJ, Gerdes K (2005) Partition-associated incompatibility caused by random assortment of pure plasmid clusters. *Mol Microbiol* 56(6):1430–1440.
8. Adachi S, Hori K, Hiraga S (2006) Subcellular positioning of F plasmid mediated by dynamic localization of SopA and SopB. *J Mol Biol* 356(4):850–863.
9. Ebersbach G, et al. (2006) Regular cellular distribution of plasmids by oscillating and filament-forming ParA ATPase of plasmid pB171. *Mol Microbiol* 61(6):1428–1442.
10. Sengupta M, Nielsen HJ, Youngren B, Austin S (2010) P1 plasmid segregation: Accurate redistribution by dynamic plasmid pairing and separation. *J Bacteriol* 192(5): 1175–1183.
11. Jha JK, Baek JH, Venkova-Canova T, Chattoraj DK (2012) Chromosome dynamics in multichromosome bacteria. *Biochim Biophys Acta* 1819(7):826–829.
12. Wang X, Montero Llopis P, Rudner DZ (2013) Organization and segregation of bacterial chromosomes. *Nat Rev Genet* 14(3):191–203.
13. Bouet JY, Stouf M, Lebailly E, Cornet F (2014) Mechanisms for chromosome segregation. *Curr Opin Microbiol* 22:60–65.
14. Val ME, Soler-Bistué A, Bland MJ, Mazel D (2014) Management of multipartite genomes: The Vibrio cholerae model. *Curr Opin Microbiol* 22:120–126.
15. Szardenings F, Guymer D, Gerdes K (2011) ParA ATPases can move and position DNA and subcellular structures. *Curr Opin Microbiol* 14(6):712–718.
16. Vecchiarelli AG, Mizuuchi K, Funnell BE (2012) Surfing biological surfaces: Exploiting the nucleoid for partition and transport in bacteria. *Mol Microbiol* 86(3):513–523.
17. Baxter JC, Funnell BE (2014) Plasmid Partition Mechanisms. *Microbiol Spectr* 2(6).
18. Ringgaard S, van Zon J, Howard M, Gerdes K (2009) Movement and equipositioning of plasmids by ParA filament disassembly. *Proc Natl Acad Sci USA* 106(46):19369–19374.
19. Hatano T, Niki H (2010) Partitioning of P1 plasmids by gradual distribution of the ATPase ParA. *Mol Microbiol* 78(5):1182–1198.
20. Ptacin JL, et al. (2010) A spindle-like apparatus guides bacterial chromosome segregation. *Nat Cell Biol* 12(8):791–798.
21. Schofield WB, Lim HC, Jacobs-Wagner C (2010) Cell cycle coordination and regulation of bacterial chromosome segregation dynamics by polarly localized proteins. *EMBO J* 29(18):3068–3081.
22. Shebelut CW, Guberman JM, van Teeffelen S, Yakhnina AA, Gitai Z (2010) Caulobacter chromosome segregation is an ordered multistep process. *Proc Natl Acad Sci USA* 107(32):14194–14198.
23. Ah-Seng Y, Rech J, Lane D, Bouet JY (2013) Defining the role of ATP hydrolysis in mitotic segregation of bacterial plasmids. *PLoS Genet* 9(12):e1003956.
24. Hatano T, Yamaichi Y, Niki H (2007) Oscillating focus of SopA associated with filamentous structure guides partitioning of F plasmid. *Mol Microbiol* 64(5):1198–1213.
25. Fogel MA, Waldor MK (2006) A dynamic, mitotic-like mechanism for bacterial chromosome segregation. *Genes Dev* 20(23):3269–3282.
26. Jakimowicz D, Zydek P, Kois A, Zakrzewska-Czerwińska J, Chater KF (2007) Alignment of multiple chromosomes along helical ParA scaffolding in sporulating Streptomyces hyphae. *Mol Microbiol* 65(3):625–641.
27. Banigan EJ, Gelbart MA, Gitai Z, Wingreen NS, Liu AJ (2011) Filament depolymerization can explain chromosome pulling during bacterial mitosis. *PLOS Comput Biol* 7(9):e1002145.
28. Ietswaart R, Szardenings F, Gerdes K, Howard M (2014) Competing ParA structures space bacterial plasmids equally over the nucleoid. *PLOS Comput Biol* 10(12): e1004009.
29. Shtylla B, Keener JP (2012) A mathematical model of ParA filament-mediated chromosome movement in Caulobacter crescentus. *J Theor Biol* 307:82–95.
30. Vecchiarelli AG, et al. (2010) ATP control of dynamic P1 ParA-DNA interactions: A key role for the nucleoid in plasmid partition. *Mol Microbiol* 78(1):78–91.
31. Lim HC, et al. (2014) Evidence for a DNA-relay mechanism in ParABS-mediated chromosome segregation. *eLife* 3:e02758.
32. Sugawara T, Kaneko K (2011) Chemophoresis as a driving force for intracellular organization: Theory and application to plasmid partitioning. *Biophysics (Oxf)* 7:77–88.
33. Hwang LC, et al. (2013) ParA-mediated plasmid partition driven by protein pattern self-organization. *EMBO J* 32(9):1238–1249.

34. Vecchiarelli AG, Seol Y, Neuman KC, Mizuuchi K (2014) A moving ParA gradient on the nucleoid directs subcellular cargo transport via a chemophoresis force. *BioArchitecture* 4(4-5):154–159.
35. Hu L, Vecchiarelli AG, Mizuuchi K, Neuman KC, Liu J (2015) Directed and persistent movement arises from mechanochemistry of the ParA/ParB system. *Proc Natl Acad Sci USA* 112(51):E7055–E7064.
36. Le Gall A, et al. (2016) Bacterial partition complexes segregate within the volume of the nucleoid. *Nat Commun* 7:12107.
37. Fiebig A, Keren K, Theriot JA (2006) Fine-scale time-lapse analysis of the biphasic, dynamic behaviour of the two Vibrio cholerae chromosomes. *Mol Microbiol* 60(5): 1164–1178.
38. Wiggins PA, Cheveralls KC, Martin JS, Lintner R, Kondev J (2010) Strong intranucleoid interactions organize the Escherichia coli chromosome into a nucleoid filament. *Proc Natl Acad Sci USA* 107(11):4991–4995.
39. Kuwada NJ, Cheveralls KC, Traxler B, Wiggins PA (2013) Mapping the driving forces of chromosome structure and segregation in Escherichia coli. *Nucleic Acids Res* 41(15): 7370–7377.
40. Javer A, et al. (2014) Persistent super-diffusive motion of Escherichia coli chromosomal loci. *Nat Commun* 5:3854.
41. Ebersbach G, Briegel A, Jensen GJ, Jacobs-Wagner C (2008) A self-associating protein critical for chromosome attachment, division, and polar organization in caulobacter. *Cell* 134(6):956–968.
42. Bowman GR, et al. (2008) A polymeric protein anchors the chromosomal origin/ParB complex at a bacterial cell pole. *Cell* 134(6):945–955.
43. Vecchiarelli AG, Hwang LC, Mizuuchi K (2013) Cell-free study of F plasmid partition provides evidence for cargo transport by a diffusion-ratchet mechanism. *Proc Natl Acad Sci USA* 110(15):E1390–E1397.
44. Sanchez A, et al. (2015) Stochastic self-assembly of ParB proteins builds the bacterial DNA segregation apparatus. *Cell Syst* 1(2):163–173.
45. Ebersbach G, Gerdes K (2001) The double par locus of virulence factor pB171: DNA segregation is correlated with oscillation of ParA. *Proc Natl Acad Sci USA* 98(26): 15078–15083.
46. Vecchiarelli AG, Neuman KC, Mizuuchi K (2014) A propagating ATPase gradient drives transport of surface-confined cellular cargo. *Proc Natl Acad Sci USA* 111(13): 4880–4885.
47. Surovtsev IV, Lim HC, Jacobs-Wagner C (2016) The slow mobility of the ParA partitioning protein underlies its steady-state patterning in Caulobacter. *Biophys J* 110(12): 2790–2799.
48. Lutkenhaus J (2012) The ParA/MinD family puts things in their place. *Trends Microbiol* 20(9):411–418.
49. Shih YL, Zheng M (2013) Spatial control of the cell division site by the Min system in Escherichia coli. *Environ Microbiol* 15(12):3229–3239.
50. Rowlett VW, Margolin W (2015) The Min system and other nucleoid-independent regulators of Z ring positioning. *Front Microbiol* 6:478.
51. Kretschmer S, Schwille P (2016) Pattern formation on membranes and its role in bacterial cell division. *Curr Opin Cell Biol* 38:52–59.
52. Kruse K, Howard M, Margolin W (2007) An experimentalist's guide to computational modelling of the Min system. *Mol Microbiol* 63(5):1279–1284.
53. Loose M, Kruse K, Schwille P (2011) Protein self-organization: Lessons from the min system. *Annu Rev Biophys* 40:315–336.
54. Thompson SR, Wadhams GH, Armitage JP (2006) The positioning of cytoplasmic protein clusters in bacteria. *Proc Natl Acad Sci USA* 103(21):8209–8214.
55. Savage DF, Afonso B, Chen AH, Silver PA (2010) Spatially ordered dynamics of the bacterial carbon fixation machinery. *Science* 327(5970):1258–1261.
56. Roberts MA, Wadhams GH, Hadfield KA, Tickner S, Armitage JP (2012) ParA-like protein uses nonspecific chromosomal DNA binding to partition protein complexes. *Proc Natl Acad Sci USA* 109(17):6698–6703.
57. Rae BD, Long BM, Badger MR, Price GD (2012) Structural determinants of the outer shell of β-carboxysomes in Synechococcus elongatus PCC 7942: Roles for CcmK2, K3-K4, CcmO, and CcmL. *PLoS One* 7(8):e43871.
58. Derman AI, Lim-Fong G, Pogliano J (2008) Intracellular mobility of plasmid DNA is limited by the ParA family of partitioning systems. *Mol Microbiol* 67(5):935–946.
59. Verdaasdonk JS, et al. (2013) Centromere tethering confines chromosome domains. *Mol Cell* 52(6):819–831.
60. White MA, Eykelenboom JK, Lopez-Vernaza MA, Wilson E, Leach DR (2008) Non-random segregation of sister chromosomes in Escherichia coli. *Nature* 455(7217): 1248–1250.
61. Lau IF, et al. (2003) Spatial and temporal organization of replicating Escherichia coli chromosomes. *Mol Microbiol* 49(3):731–743.
62. Thanbichler M, Iniesta AA, Shapiro L (2007) A comprehensive set of plasmids for vanillate- and xylose-inducible gene expression in Caulobacter crescentus. *Nucleic Acids Res* 35(20):e137.
63. Paintdakhi A, et al. (2016) Oufti: An integrated software package for high-accuracy, high-throughput quantitative microscopy analysis. *Mol Microbiol* 99(4):767–777.
64. Sliusarenko O, Heinritz J, Emonet T, Jacobs-Wagner C (2011) High-throughput, subpixel precision analysis of bacterial morphogenesis and intracellular spatio-temporal dynamics. *Mol Microbiol* 80(3):612–627.
65. Parry BR, et al. (2014) The bacterial cytoplasm has glass-like properties and is fluidized by metabolic activity. *Cell* 156(1-2):183–194.
66. Branka AC, Heyes DM (1998) Algorithms for Brownian dynamics simulation. *Phys Rev E Stat Phys Plasmas Fluids Relat Interdiscip Topics* 58(2):2611–2615.
67. Honeycutt RL (1992) Stochastic Runge-Kutta algorithms. I. White noise. *Phys Rev A* 45(2):600–603.
68. Weber SC, Spakowitz AJ, Theriot JA (2010) Bacterial chromosomal loci move subdiffusively through a viscoelastic cytoplasm. *Phys Rev Lett* 104(23):238102.
69. Leonard TA, Butler PJ, Löwe J (2005) Bacterial chromosome segregation: Structure and DNA binding of the Soj dimer–a conserved biological switch. *EMBO J* 24(2): 270–282.